RESEARCH ARTICLE

NANO · MICRO small
www.small-journal.com

The In Situ Optimization of Spinterface in Polymer Spin Valve by Electronic Phase Separated Oxides

Cheng Zhang, Shuaishuai Ding, Yuan Tian, Jing Wang, Yunzhong Chen, Tongyun Zhao, Fengxia Hu,* Wenping Hu, and Baogen Shen**

Tailoring the interface between organic semiconductor (OSC) and ferromagnetic (FM) electrodes, that is, the spinterface, offers a promising way to manipulate and optimize the magnetoresistance (MR) ratio of the organic spin valve (OSV) devices. However, the non-destructive in situ regulation method of spinterface is seldom reported, limiting its theoretical research and further application in organic spintronics. $(La_{2/3}Pr_{1/3})_{5/8}Ca_{3/8}MnO_3$ (LPCMO), a recently developed FM material, exhibits a strong electronic phase separation (EPS) property, and can be employed as an effective in situ spinterface adjuster. Herein, we fabricated a LPCMO-based polymer spin valve with a vertical configuration of LPCMO/poly(3-hexylthiophene-2,5-diyl) (P3HT)/Co, and emphasized the important role of LPCMO/P3HT spinterface in MR regulation. A unique competitive spin-scattering mechanism generated by the EPS characteristics of LPCMO inside the polymer spin valve was discovered by abstracting the anomalous non-monotonic MR value as a function of pre-set magnetic field (B_{pre}) and temperature (T). Particularly, a record-high MR ratio of 93% was achieved in polymer spin valves under optimal conditions. These findings highlight the importance of interdisciplinary research between organic spintronics and EPS oxides and offer a novel scenario for multi-level storage via spinterface manipulation.

1. Introduction

Spintronics, which is based on the giant magnetoresistance (GMR) effect discovered in 1988,[1] has become the cornerstone of modern information technology. By utilizing the spin degree freedom of carriers, the spintronics devices have counteracted the limitations in the electronics industry, showing great promise in quantum computing and data storage.[2–5] One of the most basic spintronic devices is a spin valve, which consists of two ferromagnetic (FM) electrodes decoupled by a non-magnetic (NM) interlayer.[6] The demanding fabrication procedures, such as lattice matching requirements, high-temperature treatment, and high cost, limit the application of classic spin valve, which is entirely made of inorganic materials.[7] In comparison, conjugated polymers can make up for the above deficiencies due to their unique natures of solution processability, low-cost, light weight, mechanical flexibility, and chemical

C. Zhang, B. Shen
Ningbo Institute of Materials Technology & Engineering
Chinese Academy of Sciences
Ningbo, Zhejiang 315201, China
E-mail: shenbg@iphy.ac.cn

C. Zhang, J. Wang, Y. Chen, T. Zhao, F. Hu, B. Shen
Beijing National Laboratory of Condensed Matter Physics & Institute of Physics
Chinese Academy of Sciences
Beijing 100190, China
E-mail: fxhu@iphy.ac.cn

S. Ding, W. Hu
Tianjin Key Laboratory of Molecular Optoelectronic Sciences
Department of Chemistry
Institute of Molecular Aggregation Science
Tianjin University
Tianjin 300072, China
E-mail: dingshuaishuai@tju.edu.cn

Y. Tian
School of Physics & Electronics
Hunan University
Hunan 410082, China

Y. Chen, T. Zhao, F. Hu, B. Shen
School of Physical Sciences
University of Chinese Academy of Sciences
Beijing 100049, China

F. Hu
Songshan Lake Materials Laboratory
Dongguan, Guangdong 523808, China

W. Hu
Joint School of National University of Singapore and Tianjin University
International Campus of Tianjin University
Binhai New City
Fuzhou 350207, China

B. Shen
Ganjiang Innovation Academy
Chinese Academy of Sciences
Ganzhou, Jiangxi 341000, China

The ORCID identification number(s) for the author(s) of this article can be found under https://doi.org/10.1002/smll.202303375

DOI: 10.1002/smll.202303375

tailorability.[8–11] Additionally, the innate weak spin-orbit coupling and ultrahigh spin lifetimes (≈μs) make them attractive for spin transport compared to inorganic materials.[12–17] Since the pioneering work by Xiong et al. in 2004,[18] the organic spin valve (OSV) device based on organic semiconductors (OSCs) has been attracting the interest of the scientific community and become a game changer toward the next generation spintronic devices.[19,20]

The spinterface effect, which is a spin-dependent hybrid interfacial state (SDHIS) that only existed in FM/OSC interface, can effectively modulate the spin injection efficiency.[21–27] Optimizing the device performance of OSVs through spin interface modulation is one of the primary goals of organic spintronics. The FM electrode as a spin injector that provides unbalanced spin-polarized carriers is the foundation of boosting spin injection efficiency in the OSV devices.[28,29] To date, several initiatives have been made to enhance band alignment, reduce spin-related dispersion, and optimize device performance.[30] However, the lack of in situ methods for spinterface modulation makes it challenging to assess its contribution to the entire device, which has a significant negative impact on the rapid development field. Compared with traditional metallic FM electrodes such as Fe, Co, $Ni_{81}Fe_{19}$, etc., the half-metallic perovskite oxide material $(La_{2/3}Pr_{1/3})_{5/8}Ca_{3/8}MnO_3$ (LPCMO) combines the advantages of high spin polarizability (≈97%), atomic-level flat surface, water and oxygen stability, and moderate conductivity, benefiting the construction of high-performance spintronic devices.[31–33] As a well-known electronic phase separation (EPS) material, LPCMO exhibits two coexisting electronic phases, knowing as ferromagnetic metallic (FMM) phase and antiferromagnetic charge ordered insulating (COI) phase.[34–35] More importantly, the FMM/COI ratio inside the LPCMO can be modulated by external magnetic field, which makes LPCMO electrode suitable for in situ spin-dependent interfacial regulation at the OSC/FM interface.[31–39] As far as we were concerned, the regulation patterns of the FMM-COI transformation inside the LPCMO film on the device performance were not fully demonstrated. Additionally, it was unclear how the inherent properties of the LPCMO electrode itself affected the neighboring LPCMO/polymer spinterface and the entire spin-valve signals, particularly when the device resistance was changing. Therefore, investigations into the LPCMO-based polymer spin valve and a thorough assessment of the associated spinterface would not only help to optimize the performance of the device but also extend our understanding of the physical mechanisms relating to spintronics.

Herein, based on the in situ spinterface adjustor of EPS perovskite oxide, we constructed the polymer spin valve device with a vertical configuration of LPCMO/P3HT/Co for the first time. Using our unique mechanically transferrable procedure,[40] we obtained strong and tunable spin valve signals with rapid response and steep change, avoiding the unstable working states caused by metal filaments. Under optimal spinterface, a polymer spin valve device with a maximum MR ratio of 93% was demonstrated. We recorded the anomalous non-monotonic magnetoresistance (MR) responses using the temperature- and pre-set magnetic field-dependent test technique. To the best of our knowledge, just one piece of literature documented LPCMO-based OSV devices with the organic small molecule Alq_3 serving as the spin transport layer, and only monotonic regulation patterns were shown.[36] The unique non-monotonic MR regulation in our LPCMO/polymer systems can be well explained by our proposed competitive phenomenological model. Furthermore, we discovered a direct correlation between the device performance and the LPCMO/P3HT spinterface effect, which broadens the cognitive boundaries of the pre-existing EPS-modulated spin injection model. By examining the relationship between the resistances and the MR signals of the whole device, the spin scattering competition mechanism, and the dominant role of the LPCMO/P3HT spinterface effect in polymer spin valve devices were qualitatively revealed. Our study proves that the spin-orbit coupling and conductance mismatch effect should be comprehensively considered in system engineering to improve performance of the polymer spin valve devices. These findings inspire the development of organic spintronics and offer a novel method for improving performance through spinterface tuning.

2. Results and Discussion

2.1. Device Structure and the Spinterface Adjustor LPCMO

Our vertical polymer spin valve consists of a 30 nm P3HT layer sandwiched between a 60 nm LPCMO thin film and a 10 nm cobalt thin film with a gold capping layer (see experimental section). In this polymer spin valve device, the perovskite oxide material LPCMO with high spin polarization serves as the spin injector, while Co serves as the spin detector. The π-conjugated polymer P3HT acts as the NM layer to decouple the two FM electrodes and transport the spin-polarized current. The device structure schematic diagram is shown in **Figure 1**a.

This study was designed to utilize the EPS feature of LPCMO to in situ optimize the spinterface in polymer spin valve devices, hence a thorough investigation of LPCMO itself takes precedence. The LPCMO film was deposited on a $SrTiO_3$ (STO) (001) substrate through the pulsed laser deposition (PLD) technique. As characterized by X-ray diffraction (XRD) and atomic force microscopy (AFM) shown in Figure S1 (Supporting Information), the LPCMO layer has a high quality crystal structure and atomically flat surface, which is critical for the construction of a well-defined P3HT/LPCMO spinterface. As a large-scale electronic phase separation (EPS) oxide, the coexistence of the FMM and COI phases inside LPCMO is characterized by a magnetic field-dependent test.[35,36] The physical properties of LPCMO thin film can be significantly changed by applying the pre-set magnetic fields (B_{pre}) before standard electrical and magnetic characterizations since the COI phase can be "melted" into the FMM phase under the influence of the external magnetic field (Figure 1b). The electrical transport properties of LPCMO thin film under different B_{pre} are shown in Figure 1c. When the B_{pre} increases, the COI phase is gradually replaced by the FMM phase, as revealed by the significant decrease in thin film resistance. At the same time, the anisotropic magnetoresistance (AMR) effect of LPCMO films varies little in the magnetic field sweeping range from −2 to +2 kOe. Although the resistance of the LPCMO changed from ≈1.6 to ≈75 kΩ, its AMR value, which is defined as

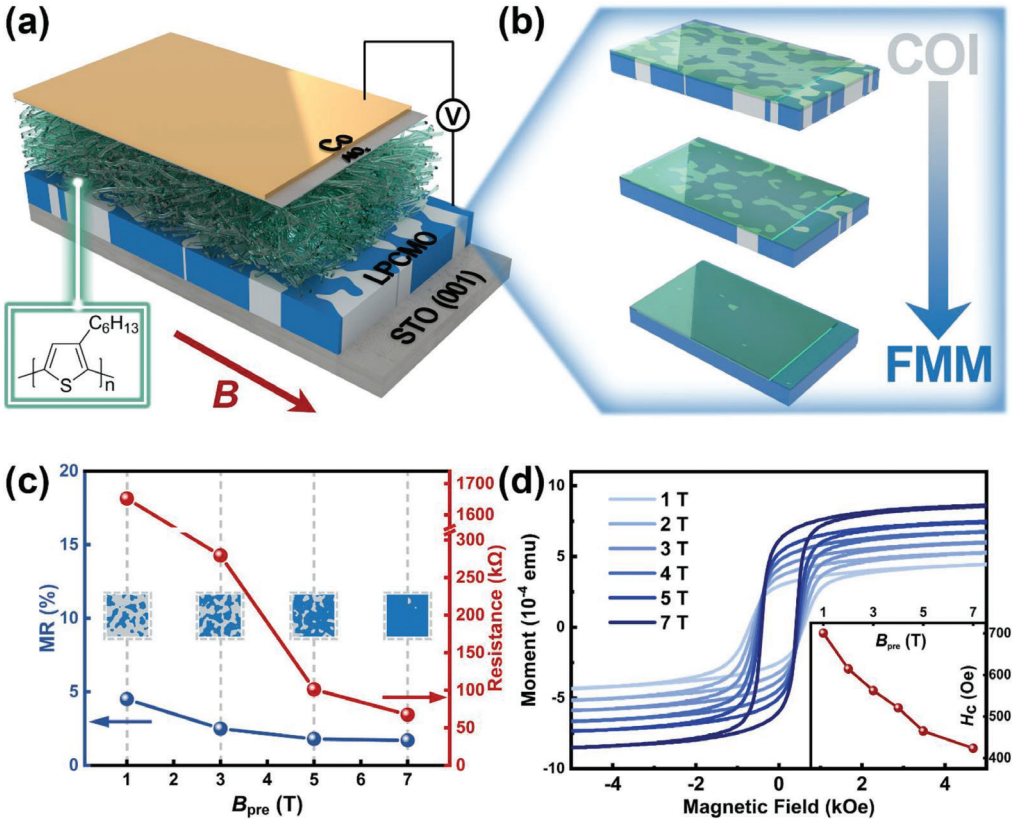

Figure 1. In situ modulation of spinterface in LPCMO-based polymer spin valve. a) The schematic diagram of the polymer spin valve device structure with vertical LPCMO/P3HT/AlO_x/Co configuration. The in-plane magnetic field (B) is applied to the device. b) The LPCMO/P3HT spinterface can be adjusted in situ by altering the FMM/COI phase transition inside the LPCMO film. The blue area represents the FMM phase, and the white area refers to the COI phase. The green area on the surface of LPCMO represents the spinterface formed by the hybridization between LPCMO and P3HT. c) The MR ratio (blue) and the resistance (red) of the LPCMO thin film as a function of the pre-set magnetic fields (B_{pre}). The insets represent the EPS degree on the LPCMO surface under different B_{pre}. d) The *M-H* curves and the coercive field (inset) of the LPCMO thin film as a function of B_{pre}. The B_{pre} was applied along the in-plane direction to the LPCMO in advance, and then removed before *M-H* and MR measurements.

MR (%) = (R_{max} − R_{min}) / R_{min} × 100%, basically remained unchanged (<5%). The detailed MR curves of LPCMO were exhibited in Figure S2 (Supporting Information). The melting of COI phase domains affects the magnetic properties of the LPCMO films as well. Figure 1d shows the magnetic hysteresis loops (*M-H*) of the LPCMO films under different B_{pre} at 10 K, as recorded after field cooling from 300 K at 500 Oe. The sample exhibits strong ferromagnetism with the rectangular shape in *M-H* loops. The saturation magnetic moment of the LPCMO film increases continuously with the increase of the B_{pre}, which indicates that the antiferromagnetic COI phase in the LPCMO film is gradually transformed into the FMM phase by the $B_{pre.}$ Since the interaction of FMM/COI in the LPCMO film has been reduced, the magnetic domains can be flipped easily using a smaller external magnetic field. This results in a continuous decrease of the coercive force (H_C) of LPCMO, and the shape of the *M-H* loop is closer to a rectangle. The temperature dependence of magnetization (*M-T*) and resistance (*R-T*) curves of the LPCMO are shown in Figure S3 (Supporting Information), which exhibits the typical FMM/COI transition of the LPCMO as a function of *T*. The FMM/COI phase competition in the LPCMO can be further used to modulate the spinterface and related magnetic responses in the following LPCMO-based polymer spin valve device.

2.2. Large and Tunable MR Signal in the Polymer Spin Valve

The MR curves of the LPCMO-based polymer spin valve as a function of B_{pre} measured at 10 K using 0.1 V voltage bias are presented in **Figure 2**a–d. The pre-set magnetic field (B_{pre}) was applied along the in-plane direction and then linearly reduced to 1 T before MR measurement. The relative magnetization orientations of the two FM layers shift from parallel (P) to antiparallel (AP) and back to parallel (P) as the sweeping in-plane magnetic field changes from 1 to −1 T and back to 1 T. As a result, the device resistance changes from R_P to R_{AP} and finally back to R_P. Usually, the MR ratio in OSV is defined as $MR = (R_{AP} - R_P)/R_P \times 100\%$. In order to facilitate the comparison between the LPCMO electrode and polymer spin valve device, here we use the basic formula, which is MR = (R_{max} − R_{min})/R_{min} × 100%, to define the MR ratio, and the R_{max} and R_{min} represent the appeared maximal and minimal resistance value in the magnetic field ranged from −2 kOe to + 2 kOe, respectively.

The device exhibits an obvious magnetic response with a typical positive MR value of 23% in the initial state (T = 10 K, B_{pre} = 1 T; Figure 2a). More importantly, the MR signal of the device can be significantly regulated by $B_{pre.}$ The device exhibits a strong spin valve effect of 80% with very sharp vertical resistance

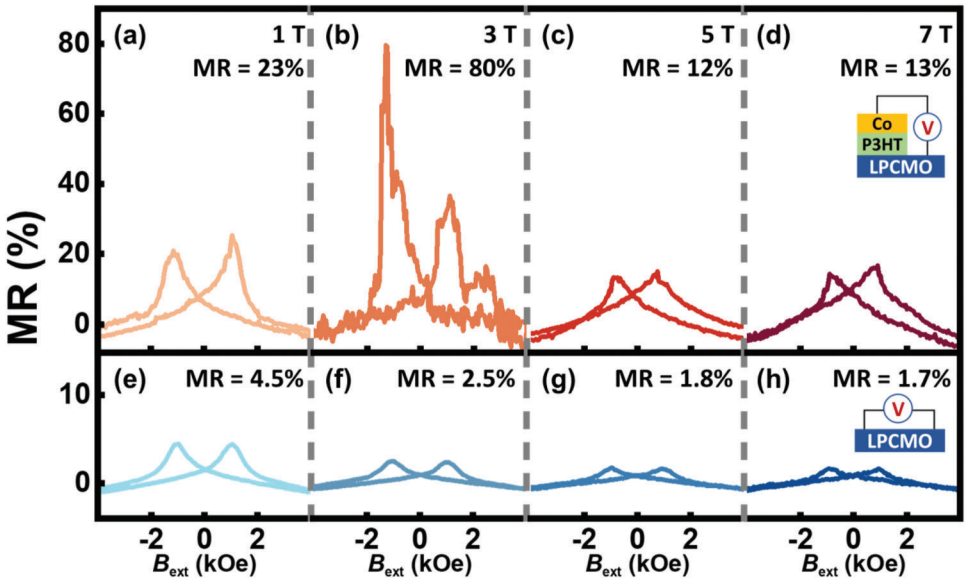

Figure 2. The MR responses at 10 K measured under different test conditions for LPCMO/P3HT/Co device and LPCMO electrode. a–d) The MR responses of LPCMO/P3HT/Co device; pre-set magnetic field B_{pre} = 1, 3, 5, and 7 T, respectively. e–h) The MR responses of LPCMO electrode; B_{pre} = 1, 3, 5, and 7 T, respectively. The insets represent the device structure. All MR measurements were performed with V = 0.1 V.

switches under a 3 T B_{pre} (Figure 2b), which is hard to achieve in nearly most OSVs. The noise signals observed in the MR curve could potentially be attributed to amorphous solid states of P3HT and residual stress at interfaces induced by spin-coating process. The maximum MR value of the device can reach up to 93% under optimized experimental condition (Figure S4a, Supporting Information). To the best of our knowledge, this is the highest MR value reported so far in the polymer spin valves (Table 1). It indicates the spin polarization enhancement effect of our unique spin-dependent hybrid LPCMO/P3HT interfacial state. This phenomenon was also observed in two other comparative devices identical to the initial device, as shown in Supplementary Note 1, Figures S5 and S6 (Supporting Information). Although the MR ratios of the device decrease slightly overall, the line shape and the variation trend of the MR curves remain basically unchanged, proving the repeatability and tunability of our polymer spin valve devices.

Table 1. Different performance parameters of polymer spin valves.

Device configuration	MR [%]	T [K]	Ref.
LPCMO/P3HT/Co	93	30	This work.
LSMO/TPP/Co	15	80	[43]
$Fe_{50}Co_{50}$/P3HT/NiFe	22	5	[44]
LSMO/D-DOO-PPV/Co	45	10	[45]
LSMO/P3MT/Co	70	20	[46]
LSMO/P3HT/AlO_x/Co	0.24	2	[47]
LSMO/P3HT/Co	15	20	[48]
LSMO/P3HT/AlO_x/Co	7	2	[40]
NiFe/P3HT/AlO_x/Co	0.2	10	[49]
LSMO/PAIID-CNTVT-C1/NiFe	25	50	[50]
LSMO/PTDCNTVT-420/Py	30	10	[51]
NiFe/PNVT-CN-8/Co	0.09	10	[52]
Fe_3O_4/P3HT/Co	2	10	[53]
NiFe/PNVT-8/Co	0.36	10	[54]

We further compare the device signal with the LPCMO electrode signal to separate the contribution from FM with EPS characteristic (Figure 2e–h). In terms of the MR ratios, the MR of the device is typically around one order of magnitude larger than the AMR of the LPCMO electrode. The line shape and amplitude of the MR curves in devices (Figure 2a–d) were obviously different from the AMR curves of the LPCMO, proving the authenticity of the GMR signal under a small B_{pre} (1 T, 3 T). On the contrary, the MR value of the device dropped fast under a large B_{pre} (B_{pre} = 5 T, Figure 2c; B_{pre} = 7 T, Figure 2d), and its line shape and amplitude resembled those of the LPCMO electrode (Figure 2g-h), which implies the MR responses of the device were greatly influenced by the AMR effect of FM electrode at large B_{pre}. The aforementioned experimental findings demonstrate that the direct contribution of the LPCMO to the device MR is extremely limited. Other redundant magnetic response effects which may cause the crosstalk noise of the effective spin signal can be excluded from further analysis in Figures S7-S9 (Supporting Information). We also measured bias voltage dependence of the device, where MR decreases with increasing bias voltage. Furthermore, the device exhibited the same variation trend for B_{pre} modulation under 0.1 and −0.1 V bias voltage, as detailed in Figures S10 and S11 (Supporting Information).

2.3. The Anomalous Non-Monotonic Change of MR

To further evaluate the regulatory mechanism of LPCMO on the LPCMO/P3HT/Co device, we summarized the MR values from the device and the single LPCMO electrode as a function

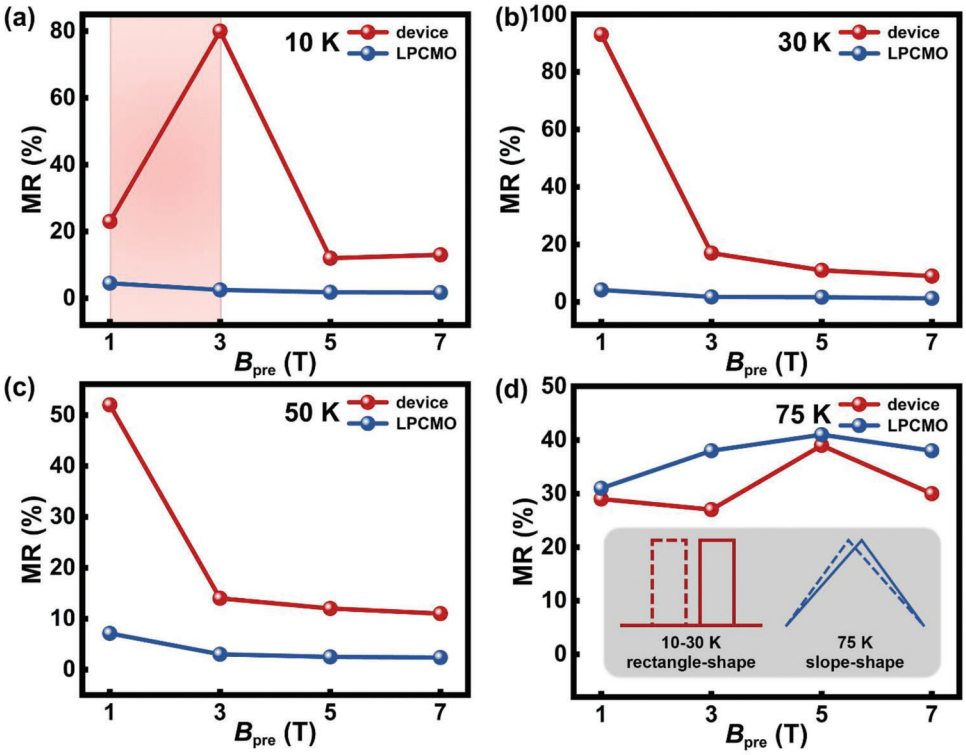

Figure 3. The anomalous non-monotonic change of MR as a function of B_{pre}. B_{pre} dependence of MR values in the LPCMO/P3HT/Co device and LPCMO electrode at a) $T = 10$ K; b) $T = 30$ K; c) $T = 50$ K; d) $T = 75$ K. The insets represent two different line shapes of the MR curves. All MR measurements were performed with $V = 0.1$ V.

of B_{pre} measured at different temperatures (**Figure 3**). The detailed MR curves were exhibited in Figures S4,S12 and S13 (Supporting Information). Generally speaking, the MR values of the LPCMO/P3HT/Co device and the LPCMO electrode differ significantly at low temperatures (10–30 K; Figure 3a,b) while tend to be consistent at high temperature (75 K; Figure 3d). And the line shape of the device has gradually changed from the typical spin-valve type of rectangle-shape to the slope-shape (Figure 3d inset), which resembles the background signal of the LPCMO electrode, proving the device signal at 75 K is mainly caused by the AMR effect of the electrode instead of the spin transport inside the OSV. At 75 K, LPCMO is in close proximity to its metal-insulator transition temperature, leading to a significant enhancement of intrinsic AMR effect inside the electrode. The detailed evaluation can be found in Table S2 (Supporting Information). By analyzing the MR curves at different temperature zones, we have demonstrated the reliability of the MR signals in low-temperature regions and elucidated the different contributions to MR response of electrodes and devices.

We further analyzed the variation of the device MR signal in the credible temperature range (10–50 K; Figure 3a-c). With the increase of B_{pre}, the MR ratio of the OSV device has been increased only in the specific interval (red area in Figure 3a, from 10 K 1T to 10 K 3T) and decreases monotonically in other intervals. The increasing MR interval corresponds well with the EPS-modulated Alq_3-based spin valve device reported by Shen et al.[36] Once the B_{pre} was applied, the FMM area in LPCMO was enlarged while the FMM/COI boundaries were reduced (Figure S14, Supporting Information). Accordingly, the spin scatterings induced by the FMM/COI boundaries will be dramatically suppressed, further facilitating the spin transport efficiency inside LPCMO thin film. Meanwhile, only the FMM phase contributes to spin polarization, so the increased FMM area contributes more to the unbalanced spin, leading to a higher bulk spin polarization (β) of LPCMO. As a result, a higher MR ratio of the whole OSV device should be expected in the B_{pre}-modulated state (Figure S14b, Supporting Information). However, we found an anomalous variation trend of the device that has not been predicted and observed in previous work. The huge difference between the LPCMO electrode and the OSV device in MR value and variation trend also indicates that the tunability in spin-valve system is not solely dominated by the LPCMO. That is, an additional competition mechanism exists.

2.4. The Spinterface Dominated Competitive Mechanism

In order to fully understand the aberrant non-monotonic change in MR ratios, a thorough analysis of the entire LPCMO/P3HT/Co device is required. We constructed a phenomenological model to analyze the overall spin injection and transport process, and the spin scattering competitive mechanism inside the polymer spin valve device was demonstrated in **Figure 4**. In the vertical organic spin valve device, spin-polarized carriers are injected from the bottom of the LPCMO electrode and collected on the top of the Co electrode, mainly experiencing five spin related processes: 1)

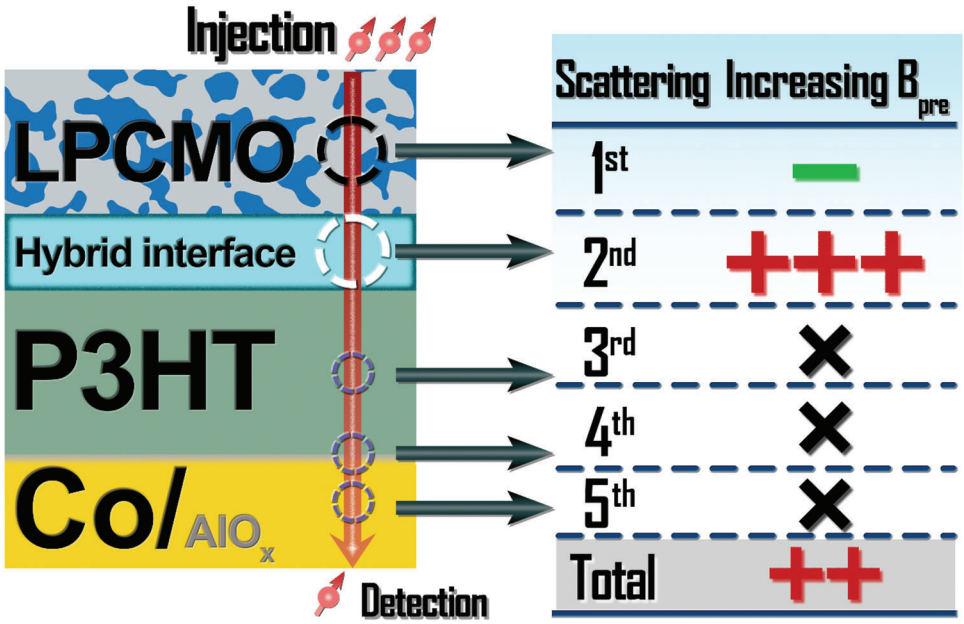

Figure 4. Phenomenological model of spin scattering competition inside the OSV device. The blue area in LPCMO represents the FMM phase, and the white area refers to the COI phase.

Inside the LPCMO electrode; 2) On the LPCMO/P3HT interface; 3) Inside the P3HT layer; 4) On the P3HT/Co interface; 5) Inside the Co electrode. Therefore, the regulation effects of the external magnetic field (B_{pre}) on the MR ratio should be determined by the sum of the above five origins. Increasing B_{pre} would reduce the scattering effect (1st scattering in Figure 4) inside the LPCMO electrode and contributes to a higher spin polarization ratio β, as we have discussed in Part 2.3. Since the P3HT and Co do not have the EPS feature, B_{pre} would not affect the scattering inside the P3HT layer, on the P3HT/Co interface, and inside the Co electrode (3rd, 4th and 5th scattering in Figure 4, respectively), the unchanged MR ratios as a function of B_{pre} in a LSMO/P3HT/Co structure (Figure S15, Supporting Information) with non-EPS electrodes has excluded the influence of 3–5 layers to the total MR with increasing B_{pre}. Therefore, we deduce the anomolous decreased MR value, which is related to the increased total spin scattering, can only be caused by the increased scattering effect on the LPCMO/P3HT interface (2nd scattering in Figure 4). This interface effect competes with the scattering effect inside the LPCMO electrode in our polymer spin valve device and plays a dominant role in the spin scattering competitive mechanism (Figure S16, Supporting Information). Hence, we can draw a conclusion that the in situ change in LPCMO/P3HT spinterface cannot be ignored. Both the spin-flip scattering in the EPS electrode and the EPS electrode/polymer spinterface effect should be taken into consideration for performance optimization in OSV devices.

Due to significant differences in band structures and transport modes between organic and inorganic materials, spin-dependent band shifts and broadening occur at van der Waals interfaces between FM/OSC layer, significantly affecting transport properties at spinterface.[22] Since this hybridization only occurs in two to three molecular layers at the interface, it is difficult to precisely measure interfacial states such as interfacial resistances and spin polarizations. Instead, we proposed a qualitative mechanism to discuss about the the two seemingly contradictory factors, spin scattering inside LPCMO and hybrid spinterface at LPCMO/P3HT interface (as is shown in Figure 4, 1st and 2nd process). It is noteworthy that under the same experimental conditions, the most significant change observed as a function of B_{pre} is the device resistance (R_{device}) and LPCMO resistance (R_{LPCMO}), while the P3HT resistance (R_{P3HT}) and Co resistance (R_{Co}) remains constant, which has already been proved in previous discussion. That is to say, the conductivity (resistance) relationship, that is, $r = \frac{R_{FM}}{R_{SC}}$, is a crucial factor in our case, which relates to the very fundamental spin transport equations known as conductivity mismatch proposed by Fert et al.[55] It refers to a situation in which two materials with different electrical conductivities are in contact with each other, resulting in a mismatch in their ability to inject spin signals, leading to charge and spin losses and reduced MR performance.

We speculate that the EPS states of LPCMO mainly affect the LPCMO/P3HT interface through the conductance mismatch that leads to an obstacle in spin injection. The B_{pre} would significantly change the resistance of LPCMO (Figure 1c) while having no effect on P3HT, hence the FMM/COI ratio of LPCMO will change the relative conductance relationship between LPCMO and P3HT. Here, we use a simple form of the conductivity mismatch formula concerning the FM/OSC contact to qualitatively explore the spin current polarization γ at the LPCMO/P3HT spinterface: [56]

$$\gamma = \beta \frac{R_{FM}}{R_{OSC}} \frac{1}{\frac{R_{FM}}{R_{OSC}} + (1-\beta^2)} = \frac{\beta r}{r + (1-\beta^2)} \quad (1)$$

where β is the bulk spin polarization of LPCMO increases as a function of B_{pre}, r is the conductivity relationship at the LPCMO and P3HT spinterface varies with B_{pre}.

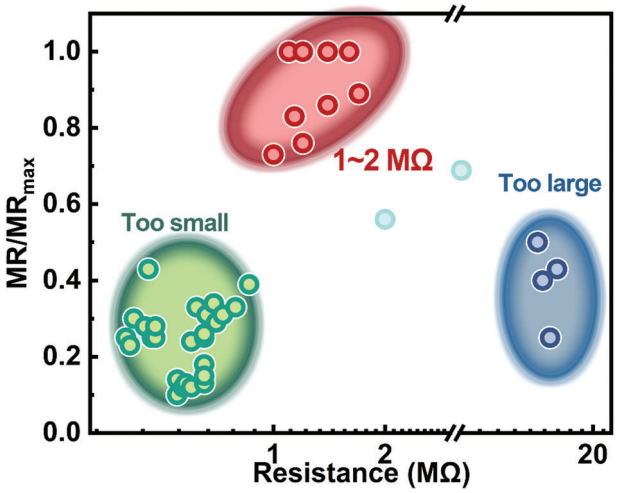

Figure 5. Calculated MR/MR_{max} as a function of the resistance of the LPCMO/P3HT/Co devices, the detailed information of all points can be found in Table S1 (Supporting Information).

It is worth noting that we use a single interface formular to discuss the overall effect on MR ratio related two interfaces is under two premises: 1) An ≈ 1 nm thick AlO_X layer was actually inserted between the Co electrode and P3HT as described in the experimental section, and such a tunnel contacts can solve the problem of the conductivity mismatch at the second P3HT/Co interface so that we could focus on the B_{pre}-related first LPCMO/P3HT interface,[57] otherwise the direct contact of low resistance Co with the P3HT should quench the spin performances and dominants the overall MR ratio regarding this model. (2) Although the conductance mismatch is not governed by device resistance, but by "spin" resistance at an (or both) interface(s) of FM and spin channel, we approximately use the bulk resistance to substitute the non-measurable interfacial resistance with considering spin diffusion length according to the relationship of $R_{FM,OSC} = \lambda_{FM,OSC}/\sigma_{FM,OSC}$.

According to the formula, we could conveniently discuss the competitive relationship between the above two contradictory factors, spin scattering inside LPCMO (β) and hybrid spinterface at LPCMO/P3HT interface (r). The mathematical simulation results (Supplementary Note 2, Figures S17–S19, Supporting Information) prove that when β increases monotonically with B_{pre}, γ can indeed show three patterns of monotonically increasing, monotonically decreasing, increasing and then decreasing as a function of r, which well corroborates our proposed competition mechanism that the conductance mismatch between LPCMO and P3HT may severely influence the spin injection efficiency during the electrical spin injection process, leading to a drastic variation in MR value.

We further demonstrate the dominant role of spin scattering in LPCMO/P3HT interface through conductance mismatch and provide additional evidence to support our phenomenological model. The relationship between the resistances of the LPCMO/P3HT/Co device and the MR signals was summarized in **Figure 5**, and all points were taken from the modulation process of one single device to ensure data consistency. A higher MR/MR_{max} value indicates that the device is functioning more effectively. The MR represents the measured MR value of the device at the particular resistance that corresponds to the horizontal axis, and the MR_{max} represents the maximum MR value achieved during the entire regulation process. Obviously, there is a direct correlation between the MR values and the resistances of the whole device. The device exhibits better performances when its total resistance is in the range of 1–2 MΩ (red area in Figure 5). While too large and too small resistances are detrimental to the device performance of the OSV (blue and green area in Figure 5, respectively).

It should be noted that the device's resistance can, to a certain extent, qualitatively mimic the effects of the conductance mismatch between the LPCMO electrode and the P3HT layer. Through the qualitative analysis of the resistance components inside the device, we can identify the specific influence of conductance mismatch effects on the MR ratio of the device (Supplementary Note 3, Figure S20, Supporting Information). These experimental results are mutually supportive of the phenomenological model we proposed, demonstrating the decisive role of the LPCMO/P3HT interface in the EPS oxide-based polymer spin valve system. Through our in situ resistance regulation of FM electrodes, we have highlighted the importance of conductivity mismatch in organic spintronic devices, which is difficult to achieve in congener systems. By utilizing the modulation effect dominated by spinterface, we can realize a stable, nonvolatile, multilevel storage function in polymer spin valve device (Supplementary Note 4, Figure S21, Supporting Information), indicating the great potential of the OSV device for the application in the field of high-density information storage and processing.

3. Conclusion

By utilizing the in situ spinterface modulation strategy, we obtained a significant MR effect of ≈93% in polymer spin valve device with vertical LPCMO/P3HT/Co structure, which is one of the best experimental results reported in polymer spin valve devices. The significant function of the EPS feature of the LPCMO in MR modulation was proved by the large and adjustable MR ratios coupled with sharp and well-defined resistance switching. Furthermore, we observed the anomalous non-monotonic response of the device to external magnetic field regulation and proposed a phenomenological model to illustrate the competitive mechanism of spin scattering in LPCMO-based polymer spin valves. We revealed the FM/OSC spinterface-dominated spin scattering mechanism, challenging prior findings that the LPCMO phase separation boundary scattering was the primary factor controlling spin injection. And this interface scattering, which is related to the conductance mismatch effect, can be exploited as a novel strategy to activate, or deactivate the working states of the OSV. This study lays the foundation for the subsequent evaluation of OSV devices with reliable magnetic response and provides diverse regulatory mechanisms in organic spintronics.

4. Experimental Section

Sample Preparation: The 60 nm bottom LPCMO thin films were deposited on a $SrTiO_3$ (STO) (001) substrate using a shadow mask with the pulsed laser deposition (PLD) technique. During deposition, the oxy-

gen atmosphere was fixed at 85 Pa, and the substrate temperature was kept at 675 °C. After the deposition process, the samples were cooled to room temperature at a rate of 10 °C min^{-1} in an oxygen atmosphere of 5×10^3 Pa. A solution of 10 mg mL^{-1} π-conjugated polymer regioregular poly (3-hexylthiophene) (RR-P3HT, TCI Chemicals) in *o*-dichlorobenzene (*o*-DCB) was filtered through a syringe filter for organic solvents and spin-coated at a rotation speed of 2000 r.p.m. over the LPCMO/STO substrate, forming a uniform 30 nm- thick polymer thin film as a spacing layer. Subsequently, the above polymer thin film was baked at 150 °C to remove the residual solvents. For top FM electrode fabrication, 10 nm Co/70 nm Au bilayer thin film was mechanically transferred onto the P3HT/LPCMO/STO structure through the originally invented PDMS-assisted technique,[40] thus avoiding the formation of uncontrollable metal filaments compared with damages from typical thermal deposition method. An ≈1 nm thick AlO_X layer was inserted between the Co electrode and P3HT. The effective area of the vertically stacked junction defined by two crossed FM electrodes was 0.5 mm × 1 mm.

Characterization and Measurement: The crystal structure of the LPCMO thin film was determined using a Bruker X-ray diffractometer (XRD) equipped with thin-film accessories (D8 Discover, Cu Kα radiation). The surface morphology and thickness were obtained using an atomic force microscope (AFM) (SPI 3800N; Seiko). Magnetic characterizations including *M-H* and *M-T* curves were performed on a superconducting quantum interference device system (SQUID, Quantum Design). All the electrical transport measurements and magnetoresistance results were obtained using a Physical Property Measurement System (PPMS Dynacool, Quantum Design) combined with Keithley 2635B Dual-Channel System Source Meter Unit (SMU).

Supporting Information

Supporting Information is available from the Wiley Online Library or from the author.

Acknowledgements

This work was supported by the National Key Research and Development Program of China (2021YFB3501202, 2020YFA0711502, 2021YFA1400300, 2019YFA0704900, 2022YFB3505201), the National Natural Sciences Foundation of China (52088101, 92263202, 52003190, 62101185, 11921004), the Strategic Priority Research Program (B, XDB33030200), the Key Program of the Chinese Academy of Sciences (CAS) and the Haihe Laboratory of Sustainable Chemical Transformations. The authors were thankful to Prof. H.C. Ren for the discussions on theoretical modeling aspects in revision.

Conflict of Interest

The authors declare no conflict of interest.

Data Availability Statement

The data that support the findings of this study are available from the corresponding author upon reasonable request.

Keywords

electronic phase separation, perovskite oxides, polymer spin valves, spinterface, spintronics

Received: April 21, 2023
Revised: May 23, 2023
Published online: June 1, 2023

[1] G. Binasch, P. Grünberg, F. Saurenbach, W. Zinn, *Phys. Rev. B* **1989**, *39*, 4828.
[2] I. Žutić, J. Fabian, S. Das Sarma, *Rev. Mod. Phys.* **2004**, *76*, 323.
[3] L. E. Hueso, J. M. Pruneda, V. Ferrari, G. Burnell, J. P. Valdés-Herrera, B. D. Simons, P. B. Littlewood, E. Artacho, A. Fert, N. D. Mathur, *Nature* **2007**, *445*, 410.
[4] V. A. Dediu, L. E. Hueso, I. Bergenti, C. Taliani, *Nat. Mater.* **2009**, *8*, 707.
[5] A. J. Drew, J. Hoppler, L. Schulz, F. L. Pratt, P. Desai, P. Shakya, T. Kreouzis, W. P. Gillin, A. Suter, N. A. Morley, V. K. Malik, A. Dubroka, K. W. Kim, H. Bouyanfif, F. Bourqui, C. Bernhard, R. Scheuermann, G. J. Nieuwenhuys, T. Prokscha, E. Morenzoni, *Nat. Mater.* **2009**, *8*, 109.
[6] D. Sun, E. Ehrenfreund, Z. Valy Vardeny, *ChemComm* **2014**, *50*, 1781.
[7] A. Privitera, M. Righetto, F. Cacialli, M. K. Riede, *Adv. Opt. Mater.* **2021**, *9*, 2100215.
[8] Z. Ni, H. Wang, H. Dong, Y. Dang, Q. Zhao, X. Zhang, W. Hu, *Nat. Chem.* **2019**, *11*, 271.
[9] S. Duan, X. Gao, Y. Wang, F. Yang, M. Chen, X. Zhang, X. Ren, W. Hu, *Adv. Mater.* **2019**, *31*, 1807975.
[10] K. Nakano, Y. Kaji, K. Tajima, *Small* **2022**, 2205570.
[11] G. Pan, L. Hu, S. Su, J. Yuan, T. Li, X. Xiao, Q. Chen, F. Zhang, *ACS Appl. Mater. Interfaces* **2020**, *12*, 29487.
[12] G. Szulczewski, S. Sanvito, M. Coey, *Nat. Mater.* **2009**, *8*, 693.
[13] X. Sun, A. Bedoya-Pinto, R. Llopis, F. Casanova, L. E. Hueso, *Appl. Phys. Lett.* **2014**, *105*, 083302.
[14] S. Sanvito, *Nat. Mater.* **2007**, *6*, 803.
[15] A. Banerjee, A. J. Pal, *Small* **2018**, *14*, 1801510.
[16] M. Wei, X. Lu, J. Qiao, S. Ren, X.-T. Hao, W. Qin, *ACS Nano* **2022**, *16*, 13049.
[17] Z. Shang, T. Liu, Q. Yang, S. Cui, K. Xu, Y. Zhang, J. Z. Deng, T. X. Wang, *Small* **2022**, *18*, 2203015.
[18] Z. H. Xiong, D. Wu, Z. Valy Vardeny, J. Shi, *Nature* **2004**, *427*, 821.
[19] X. Sun, S. Vélez, A. Atxabal, A. Bedoya-Pinto, S. Parui, X. Zhu, R. Llopis, F. Casanova, L. E. Hueso, *Science* **2017**, *357*, 677.
[20] L. Guo, X. Gu, X. Zhu, X. Sun, *Adv. Mater.* **2019**, *31*, 1805355.
[21] S. Sanvito, *Nat. Phys.* **2010**, *6*, 562.
[22] M. Galbiati, S. Tatay, C. Barraud, A. V. Dediu, F. Petroff, R. Mattana, P. Seneor, *MRS Bull.* **2014**, *39*, 602.
[23] D. Sun, M. Fang, X. Xu, L. Jiang, H. Guo, Y. Wang, W. Yang, L. Yin, P. C. Snijders, T. Z. Ward, Z. Gai, X. G. Zhang, H. N. Lee, J. Shen, *Nat. Commun.* **2014**, *5*, 4396.
[24] D. Yu, S. Ding, J. Li, W. Mi, Y. Tian, W. Hu, *J. Mater. Chem. C* **2022**, *10*, 2608.
[25] S. Liang, H. Yang, H. Yang, B. Tao, A. Djeffal, M. Chshiev, W. Huang, X. Li, A. Ferri, R. Desfeux, S. Mangin, D. Lacour, M. Hehn, O. Copie, K. Dumesnil, Y. Lu, *Adv. Mater.* **2016**, *28*, 10204.
[26] D. Sun, L. Yin, C. Sun, H. Guo, Z. Gai, X. G. Zhang, T. Z. Ward, Z. Cheng, J. Shen, *Phys. Rev. Lett.* **2010**, *104*, 236602.
[27] X. Sun, A. Bedoya-Pinto, Z. Mao, M. Gobbi, W. Yan, Y. Guo, A. Atxabal, R. Llopis, G. Yu, Y. Liu, A. Chuvilin, F. Casanova, L. E. Hueso, *Adv. Mater.* **2016**, *28*, 2609.
[28] J. Devkota, R. Geng, R. C. Subedi, T. D. Nguyen, *Adv. Funct. Mater.* **2016**, *26*, 3881.
[29] X. Chen, W. Mi, *J. Mater. Chem. C* **2021**, *9*, 9400.
[30] S. Ding, Y. Tian, W. Hu, *Nano Res.* **2021**, *14*, 3653.
[31] D. Li, G. Yu, *Adv. Funct. Mater.* **2021**, *31*, 2100550.
[32] H.-Y. Zhai, J. X. Ma, D. T. Gillaspie, X. G. Zhang, T. Z. Ward, E. W. Plummer, J. Shen, *Phys. Rev. Lett.* **2006**, *97*, 167201.
[33] T. Z. Ward, S. Liang, K. Fuchigami, L. F. Yin, E. Dagotto, E. W. Plummer, J. Shen, *Phys. Rev. Lett.* **2008**, *100*, 247204.
[34] L. Zhang, C. Israel, A. Biswas, R. L. Greene, A. de Lozanne, *Science* **2002**, *298*, 805.
[35] M. Uehara, S. Mori, C. H. Chen, S. W. Cheong, *Nature* **1999**, *399*, 560.

[36] W. Yang, Q. Shi, T. Miao, Q. Li, P. Cai, H. Liu, H. Lin, Y. Bai, Y. Zhu, Y. Yu, L. Deng, W. Wang, L. Yin, D. Sun, X. G. Zhang, J. Shen, *Nat. Commun.* **2019**, *10*, 3877.
[37] H. Lin, H. Liu, L. Lin, S. Dong, H. Chen, Y. Bai, T. Miao, Y. Yu, W. Yu, J. Tang, Y. Zhu, Y. Kou, J. Niu, Z. Cheng, J. Xiao, W. Wang, E. Dagotto, L. Yin, J. Shen, *Phys. Rev. Lett.* **2018**, *120*, 267202.
[38] T. Miao, L. Deng, W. Yang, J. Ni, C. Zheng, J. Etheridge, S. Wang, H. Liu, H. Lin, Y. Yu, Q. Shi, P. Cai, Y. Zhu, T. Yang, X. Zhang, X. Gao, C. Xi, M. Tian, X. Wu, H. Xiang, E. Dagotto, L. Yin, J. Shen, *Proc. Natl. Acad. Sci. U.S.A.* **2020**, *117*, 7090.
[39] F. Lan, H. Chen, H. Lin, Y. Bai, Y. Yu, T. Miao, Y. Zhu, T. Z. Ward, Z. Gai, W. Wang, L. Yin, E. W. Plummer, J. Shen, *Proc. Natl. Acad. Sci. U.S.A.* **2019**, *116*, 4141.
[40] S. Ding, Y. Tian, H. Wang, Z. Zhou, W. Mi, Z. Ni, Y. Zou, H. Dong, H. Gao, D. Zhu, W. Hu, *ACS Nano* **2018**, *12*, 12657.
[41] S. Watanabe, K. Ando, K. Kang, S. Mooser, Y. Vaynzof, H. Kurebayashi, E. Saitoh, H. Sirringhaus, *Nat. Phys.* **2014**, *10*, 308.
[42] T. S. Santos, J. S. Lee, P. Migdal, I. C. Lekshmi, B. Satpati, J. S. Moodera, *Phys. Rev. Lett.* **2007**, *98*, 016601.
[43] W. Xu, G. J. Szulczewski, P. LeClair, I. Navarrete, R. Schad, G. Miao, H. Guo, A. Gupta, *Appl. Phys. Lett.* **2007**, *90*, 072506,.
[44] D. Dhandapani, A. Rao, N. A. Morley, A. Das, M. Grell, M. R. J. Gibbs, *J. Appl. Phys.* **2009**, *105*, 07C702.
[45] T. D. Nguyen, G. Hukic-Markosian, F. Wang, L. Wojcik, X.-G. Li, E. Ehrenfreund, Z. V. Vardeny, *Nat. Mater.* **2010**, *9*, 345.
[46] R. Geng, A. Roy, W. Zhao, R. C. Subedi, X. Li, J. Locklin, T. D. Nguyen, *Adv. Funct. Mater.* **2016**, *26*, 3999.
[47] S. Ding, Y. Tian, Y. Li, W. Mi, H. Dong, X. Zhang, W. Hu, D. Zhu, *ACS Appl. Mater. Interfaces* **2017**, *9*, 15644.
[48] R. Geng, R. C. Subedi, H. M. Luong, M. T. Pham, W. Huang, X. Li, K. Hong, M. Shao, K. Xiao, L. A. Hornak, T. D. Nguyen, *Phys. Rev. Lett.* **2018**, *120*, 086602.
[49] S. Ding, Y. Tian, H. Dong, D. Zhu, W. Hu, *ACS Appl. Mater. Interfaces* **2019**, *11*, 11654.
[50] D. Li, X. Wang, Z. Lin, Y. Zheng, Q. Jiang, N. Zheng, W. Zhang, K.-j. Jin, G. Yu, *ACS Appl. Mater. Interfaces* **2019**, *11*, 30089.
[51] Y. Zheng, Y. Feng, D. Gao, N. Zheng, D. Li, L. Jiang, X. Wang, K. Jin, G. Yu, *Adv. Electron. Mater.* **2019**, *5*, 1970065.
[52] N. Zheng, X. Wang, Y. Zheng, D. Li, Z. Lin, W. Zhang, K.-j. Jin, G. Yu, *Adv. Mater. Interfaces* **2020**, *7*, 2000868.
[53] S. Ding, Y. Tian, X. Liu, Y. Zou, H. Dong, W. Mi, W. Hu, *Nano Res.* **2021**, *14*, 304.
[54] N. Zheng, Z. Lin, Y. Zheng, D. Li, J. Yang, W. Zhang, L. Wang, G. Yu, *Org. Electron.* **2020**, *81*, 105684.
[55] A. Fert, H. Jaffrès, *Phys. Rev. B* **2001**, *64*, 184420.
[56] T. Taniyama, E. Wada, M. Itoh, M. Yamaguchi, *NPG Asia Mater.* **2011**, *3*, 65.
[57] E. I. Rashba, *Phys. Rev. B* **2000**, *62*, R16267.